Error Sensitivity Flexibility Compensation of Joints for Improving the Positioning Accuracy of Industrial Robots

Yingjie Li, Guanbin Gao, *Member, IEEE*, Jing Na, *Member, IEEE*, and Yashan Xing, *Member, IEEE*

***Abstract*— Flexibility models based on the virtual joint approach (VJA) are essential for error compensation to improve the positioning accuracy of industrial robots across a range of payloads. However, current flexibility models are not accurate enough due to less consideration of deformation, or incorporate too many factors leading to difficulties in practical applications. This paper proposes a flexibility model based on the error sensitivity analysis to improve the positioning accuracy and stability of industrial robots. First, the effects of the six directions flexible deformation of the joint on the positioning error are analyzed by introducing the Sobol's method. It indicates that the rotational deformations around X, Y and Z-axes cause the majority of positioning errors, and only a tiny minority is originated from translational deformations along X, Y, and Z-axes. Then, a mapping equation between the flexible deformations around X, Y and Z-axes and the positioning error is derived based on this observation. Finally, a flexibility model for N degrees of freedom (DoF) industrial robots is established and an identification method is presented for flexibility coefficients. The verification experiments are performed on a 6-DoF robot, and an application example is provided for error compensation in robotic assembly tasks. The experimental results show that the proposed model has higher accuracy and stability but lower calculation cost than conventional models. Moreover, after compensation, the pose error is reduced to 0.1mm and 0.03° meeting the assembly requirements in the application example.**

***Note to Practitioners*—The joint deformation under payload and link gravity is mainly responsible for the degraded positioning accuracy of industrial robots. Error compensation by flexibility models is an effective way to improve positioning accuracy. Traditional 6-DoF flexibility models are too complex to be used in industrial scenarios, while 1-DoF flexibility models are not accurate enough. This paper proposes an error sensitivity flexibility compensation that considers the main factors affecting the positioning error, while removing factors with less impact. Compared with traditional models, the proposed model combines both high accuracy and applicability. Through establishing the mathematical equation between the joint deformation and the positioning error, a new flexibility model is derived, and an easy-to-implement method is provided to identify flexibility coefficients. The proposed model can be used conveniently for high-precision compensation of errors, including applications with constant payloads, such as assembly, cutting and welding, as well as tasks with variable payloads, such as milling, drilling and de-burring. In addition, the model can also be used to optimize poses to reduce robot flexibility and enhance resistance to deformation in one workspace. Experiments indicate that high compensation accuracy can be obtained by applying the flexibility model to robot assembly tasks.**

***Index Terms*— Positioning accuracy, flexibility error, sensitivity analysis, industrial robot.**

Manuscript received 8 January 2024; revised 24 April 2024; accepted 18 June 2024. This article was recommended for publication by Associate Editor J. Li and Editor H. Moon upon evaluation of the reviewers' comments. This work was supported in part by the National Natural Science Foundation of China under Grant 52265001 and Grant 62273169 and in part by Yunnan Fundamental Research Projects under Grant 202101AS070107 and Grant 202001AV070001. *(Corresponding author: Guanbin Gao.)*

The authors are with the Faculty of Mechanical and Electrical Engineering, Kunming University of Science and Technology, Kunming 650500, China, and also with Yunnan International Joint Laboratory of Intelligent Control and Application of Advanced Equipment, Kunming 650500, China (e-mail: yjli@stu.kust.edu.cn; gbgao@kust.edu.cn; najing25@kust.edu.cn; yashan.xing@kust.edu.cn).

Color versions of one or more figures in this article are available at https://doi.org/10.1109/TASE.2024.3419105.

Digital Object Identifier 10.1109/TASE.2024.3419105

I. Introduction

THE integration of industrial robots and artificial intelligence is driving the current comprehensive development of manufacturing. Industrial robots are the most promising equipment in smart manufacturing due to their low cost, high repeatability and good scalability in advanced applications [1], [2], [3], [4] such as milling, complex surface polishing, and precision assembly. Although the open-loop structures of industrial robots provide dexterous degrees of freedom and large workspaces, those structures also lead to insufficient stiffness, typically only 1/30-1/50 of computer numerical control (CNC) machine tools [5]. This makes robots prone to deformation under payloads, which deteriorates positioning accuracy and severely restricts their application in high-precision scenarios. Currently, the most widely used method to improve accuracy of robots is to reduce deformation via stiffness/flexibility models, e.g., off-line/on-line compensation [6], [7] and pose optimization [8], [9]. As a result, accurate and practical stiffness modeling is critical to address the deformation, which has attracted significant research attentions.

Methods of stiffness modeling for industrial robots mainly include three categories: finite element analysis (FEA), matrix structure analysis (MSA) and virtual joint approach (VJA). The FEA [10] analyzes the robot's stiffness by decomposing the physical model on a number of rather small (finite) elements, where the whole mechanical structure with the true dimension and shape of the robot is considered such that the accuracy of the stiffness model is high. However, the stiffness model by FEA needs to be recalculated when the robot configuration changes. Based on the ideas of the FEA, the MSA [11] divides

the robot structure into large flexible elements such as links, actuated and passive joints. Since joint variables are involved in the stiffness matrix, the stiffness under varying configurations can be described without recalculation. Similar to the FEA, the MSA has high accuracy and is convenient for robots with complex topologies. However, those methods described above require heavy computation and the large dimension of the stiffness model makes parameter identification difficult.

To reduce computational expenses, some work has been carried out to explore the VJA to model the stiffness of serial and parallel industrial robots. Salisbury first applied the VJA to model the stiffness of industrial robots [12], in which links are treated as rigid, while joints are flexible components. The flexible joints is described by a virtual spring between the adjacent links. Based on Salisbury's work, Chen and Kao [13] proved that the basic stiffness model does not follow the conservation of elastic potential energy. According to the conservative congruent transformation (CCT), an enhanced stiffness model (CCT model) was obtained by introducing a complementary stiffness. Alici and Shirinzadeh [14] validated the effectiveness of the CCT model on the Motoman 120 Robot. Dumas et al. [15] identified the stiffness coefficients of a six-revolute industrial robot and concluded that supplementary stiffness can be neglected in the non-singular space of the robot. In these studies, only the deformation around the joint axis is considered and other non-axial deformations and link deformations are ignored, which results in limited accuracy of the stiffness/flexibility model. Subsequently, Pashkevich [16] and Kimchik et al. [17] extended the basic model by adding a 6-DoF virtual spring between links to characterize the deformation of joints/links. In [18], the stiffness model of a Kuka robot with a gravity compensator was established by the 6-DoF virtual spring, which can accurately describes the rotational and translational deformation of joints/links. However, with increasing accuracy, the model becomes more complicated. For a 6-DoF industrial robot, there are more than 200 stiffness parameters. These parameters are obtained from FEA or identified after being simplified by special constraints, which brings difficulties in practical applications. As a result, the stiffness/flexibility models that only consider one direction deformation are widely used in recent studies for deformation error compensation [7], [19] as well as stiffness-based pose optimization [9], [20]. This indicates that the model including the 6-dimensional deformations of joints/links is more complicated for applications, in terms of high computational complexity and the difficult parameter identification. In summary, traditional stiffness/flexibility models either are overly simplistic with limited accuracy, or contain too many variables that result in the difficulties in industrial applications. Therefore, exploring stiffness/flexibility models with high accuracy that facilitate practical applications is the key in reducing flexible errors.

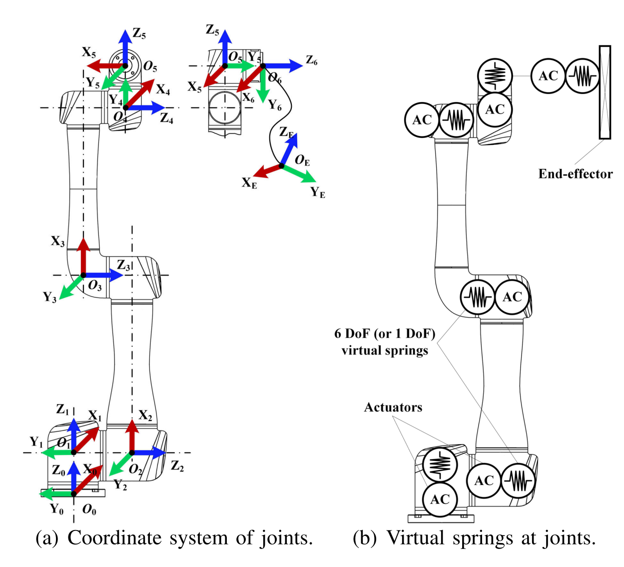
Motivated by this observation, this paper proposes an accurate and lightweight flexibility model for industrial robots. First, the effect of 6 deformations at the joint on the positioning error is investigated by introducing sensitivity analysis. The most influential deformations are retained while minor factors are eliminated. Then, a new flexibility model is established based on the main deformations with a small number of parameters needed to be identified. To build deformation mapping from the joint to positioning error, an extend deformation equation for the arbitrary joint axis is derived by using the Rodrigues's transform, where the condition that the traditional Jacobian matrix can only address deformation mapping in the Z-axis can be avoided. Furthermore, according to the established mapping equation and the linear flexibility assumption, the flexibility model incorporating the main factors is built. Finally, an identification method for flexibility coefficients is proposed and validated by the practical 6-DoF robot. The main contributions of this paper are summarized as follows:

1) A method to analyze the affect weights of the deformation components at the joints of industrial robots on the positioning error based on the error sensitivity is proposed, by which the main affect factors of the positioning error are determined.
2) A new flexibility model of joints with high accuracy and easily identifiable parameters is proposed by considering main dominant factors, which solves the limitation that the traditional kinematic Jacobian matrix can only map the axial deformation.
3) An error compensation strategy is constructed by the proposed flexibility model to reduce the positioning error of industrial robots. Experiments and an application case on assembly tasks show that the proposed method effectively improves the pose accuracy and stability.

The rest of this paper is organized as follows: In Section II, the effect of flexible deformations of virtual spring on positioning errors is analyzed. In Section III, the deformation mapping equation is derived, and a more lightweight flexibility model with high precision is established. In Section IV, experiments and an application in robotic assembly are carried out to validate the efficacy of the presented model and compensation approaches. Conclusions are drawn in Section V.

II. Effect of Flexible Deformation at Joint on Positioning Error

The positioning accuracy of industrial robots degrades as the end payload increases due to flexible deformations originated from the base, links, actuators and reducers. Using a VJA-based flexibility model to compensate errors or optimize poses can effectively improve the positioning accuracy of robots. In the VJA, flexible components can be equivalent to virtual springs between links and the actuator as shown in Fig. 1(b), and all deformations are characterized by the virtual springs. The VJA-based stiffness/flexibility models mainly include two categories. The first one assumes that the deformation at joints occurs only in the joint axis and is described by 1-DoF virtual springs [12], [13], [14], [15]. The model has a simple form and fewer parameters for identification, which is favored in practical applications, but its accuracy is limited. The second one is more accurate by considering the deformation of virtual springs in 6 directions [16], [17], [18]. However, the transfer matrix between links increases dimensionality, which requires a large number of calculations and makes parameter identification difficult, frequently with the aid of FEMs. Adopting this model to error compensation



(a) Coordinate system of joints. (b) Virtual springs at joints.

Fig. 1. The establishment of coordinate system by the modified Denavit-Hartenberg (MD-H) method [21].

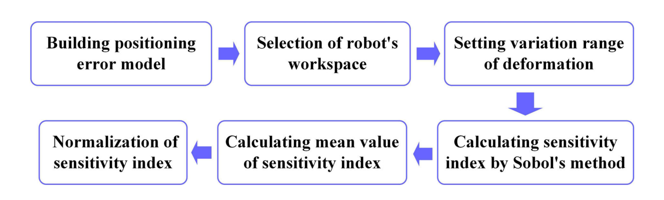
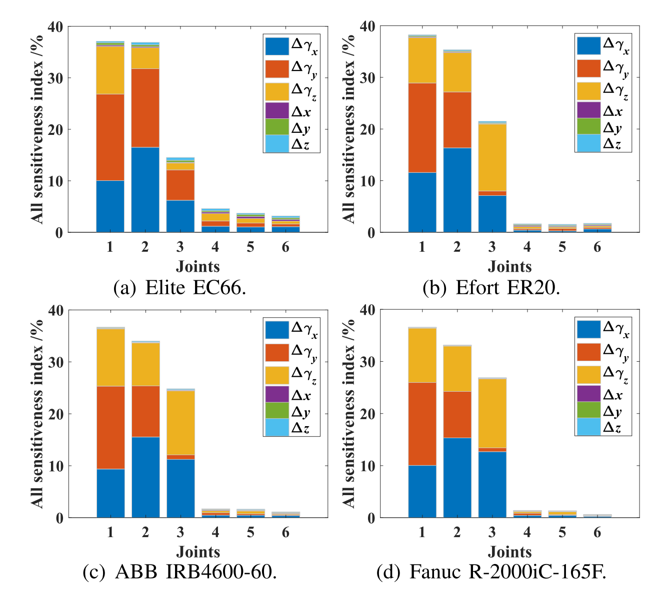


Fig. 2. Sensitivity analysis for flexible deformation.



(a) Elite EC66. (b) Efort ER20. (c) ABB IRB4600-60. (d) Fanuc R-2000iC-165F.

Fig. 3. The sensitivity index of deformation at each joint for four industrial robots. $\Delta\gamma_x$, $\Delta\gamma_y$, $\Delta\gamma_z$, Δx, Δy, Δz represent three rotational deformations and three linear deformations, respectively.

and pose optimization becomes challenging. Therefore, it is crucial to develop a flexibility model that can guarantee accuracy and has a simple form for convenient implementation in practical applications. Through error sensitivity analysis, the joint deformation factors that have the dominant influence on the robot positioning errors are determined (in Section II). Then, a flexibility error model is established for compensation (in Section III) to improve robot the positioning accuracy (in Section IV). Then, these deformations that are dominant factors are selectively retained in the modeling, while the deformations with less effect are eliminated. In this way, the complexity of the model can be effectively reduced while maintaining model accuracy.

To determine the main factors, the effect of 6 deformations for each joint on the positioning error needs to be analyzed. Nevertheless, there are no definite methods available for analyzing the contribution of joint deformation at present. This paper constructs an approach based on Sobol sensitivity analysis [22], [23]. The Sobol's method is a variance-based global sensitivity analysis, which can measure sensitivity of all variables simultaneously. According to sensitivity indices, the contribution of each deformation can be indicated clearly. Then, the most important factors affecting the positioning error can be determined. The procedure of the proposed analysis method is shown in Fig. 2. First, an error model for analyzing, $\|\Delta \boldsymbol{p}\|_2 = f(\boldsymbol{\theta}, \Delta\boldsymbol{\vartheta})$, is built by means of the rigid and deformed kinematics equations (reference to Appendix I). The rigid equation describing the case without deformation in Fig. 1(a) is obtained from the MD-H method [21]. The deformed equation can be built as shown in (30) by considering the flexible deformation $\Delta\boldsymbol{\vartheta}$. Second, a workspace needs to be selected to generate different configurations of robots. The analysis results will be more objective the more configurations there are. Next, a reasonable variation range is set, which is used to generate the variance of each deformation. Through the Sobol's method, the sensitivity index of each deformation can be calculated. Since the sensitivity index changes with the robot's configurations, their mean values are calculated as the final index. Finally, the contribution of each deformation can be obtained by normalization (0 to 1) for sensitivity index.

Based on the proposed analysis method, four general industrial robots with 6-DoF, Elite EC66, Efort ER20, ABB4600-60 and Fanuc R-2000iC-165F, are analyzed. A workspace is selected to satisfy all 4 robots, i.e., [-180°, 180°], [-90°, 65°], [-75°, 75°], [-180°, 180°], [-125°, 120°] and [-180°, 180°]. In the workspace, 1000 configurations are selected randomly. The variation of rotational deformation ($\Delta\gamma_x$, $\Delta\gamma_y$, $\Delta\gamma_z$) and translational deformation (Δx, Δy, Δz) is set to [-0.001rad, 0.001rad] and [-0.1mm, 0.1mm], respectively. The sensitivity indexes of each parameter under 1000 configurations are calculated in turn by the Sobol's method. Then, 1000 values of sensitivity index are obtained for each direction deformation. After averaging and normalizing operation, one value for each deformation is obtained. Sensitivity indexes of 6 deformations for four robots are shown in Fig. 3. The results show that rotational deformation at joints is more sensitive to the positioning error than translational deformation, which indicates the contribution of rotational deformation on the positioning error is greater. Furthermore, the percentage of sensitivity index to rotational and translational deformation are calculated as shown in Table I. For the Elite robot, the rotational deformation accounts for 93.94% of the positioning error, and the percentage rises with the size of the robot structure as well. For the Fanuc robot with large structure size (maximum working radius 2655 mm), it will reach

TABLE I
THE SENSITIVITY PERCENTAGES OF ROTATIONAL AND TRANSLATIONAL DEFORMATION FOR THE FOUR ROBOTS

	Elite EC66	Efort ER20	ABB4600	Fanuc2000iC
Maximum W_r	914mm	1722mm	2371mm	2655mm
Rotation	93.94%	96.76%	97.85%	98.77%
Translation	6.06%	3.24%	2.15%	1.23%

Note: W_r represents the working radius of industrial robots.

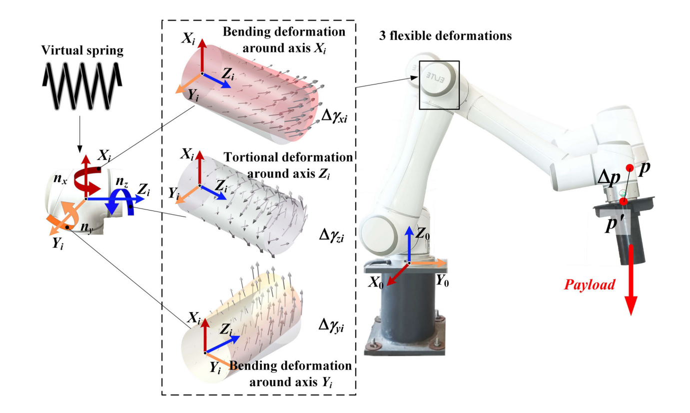
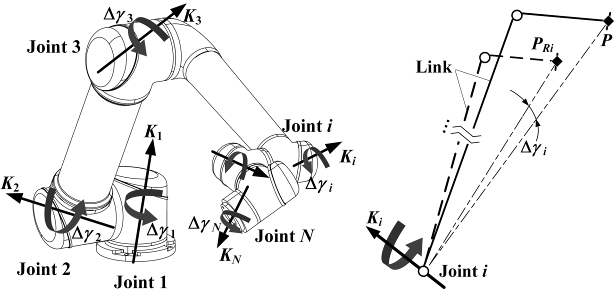


Fig. 4. Torsional and bending deformation at the joint.

98.77%. Therefore, rotational deformation is the dominant factor leading to robot end positioning error. The accuracy of the flexibility model can be ensured by retaining rotational deformation, while the model can be simplified by removing translational deformation. It is worth noting that while the rotational deformations $\Delta\gamma$ of the last three joints show lower sensitivity index compared to the first three joints in Fig. 3, joint rotational deformations $[\Delta\gamma_x, \Delta\gamma_y, \Delta\gamma_z]^{\mathrm{T}} = \boldsymbol{C}\boldsymbol{J}^{\mathrm{T}}\boldsymbol{w}$ are still affected by robot configuration $\boldsymbol{J}$, joint stiffness/flexibility $\boldsymbol{C}$ and force direction $\boldsymbol{w}$ [5], [7]. To ensure the compensation accuracy, the rotational deformations of six the joints should be considered in practical applications.

III. ERROR MODEL OF JOINT FLEXIBLE DEFORMATION

According to the analysis in Section II, rotational deformations are the primary factor of the positioning error. As shown in Fig. 4, the torque $\boldsymbol{n}_x$, $\boldsymbol{n}_y$ and $\boldsymbol{n}_z$ applied on the joint under a payload cause three rotational deformations of the virtual spring, i.e., bending deformation $\Delta\gamma_{xi}$ around the X_i-axis, torsional deformation $\Delta\gamma_{zi}$ around the Z_i-axis and bending deformation $\Delta\gamma_{yi}$ around the Y_i-axis. Due to transmission by links, these three deformations will make the robot's end to shift from the command position $\boldsymbol{p}$ to the actual position $\boldsymbol{p}'$, resulting in a positioning error $\Delta\boldsymbol{p}$. In this section, a new flexibility model is developed to describe the flexible deformation error of industrial robots based on these three deformations. First, a mathematical equation is derived to build the mapping relationship between deformation around arbitrary axis of joints and the positioning error. Then, the flexibility model is established using the torque-deformation assumption and the derived deformation mapping equation. At last, a method for determining the flexibility coefficients is presented.



(a) Rotational axis and deformation of each joint. (b) Displacement due to the deformation of joint i.

Fig. 5. Rotational deformation around arbitrary axis at joints of the robot.

A. Mapping Between Rotational Deformation and End Positioning Error

The mapping equation between rotational deformation and the positioning error is generally obtained by numerical calculation [17], which has limited accuracy and unstable computational results. It has also been mentioned that the mapping equation can be derived by the screw theory [18], but no specific mathematical equation is given. In this paper, a mapping equation is derived by using the homogenous transformation matrix. Without loss of generality, it is assumed that the deformation at the joint is around arbitrary axis, not limited to the X, Y or Z-axes. As shown in Fig. 5(a), there is a deflection angle $\Delta\gamma_i$ at each joint i, and the corresponding rotation axis is $\boldsymbol{K}_i$ which is an identity vector. The deformation of each joint makes the end position displaced. Specifically, the deformation at joint 1 causes the end position $\boldsymbol{p}$ to rotate $\Delta\gamma_1$ around $\boldsymbol{K}_1$. The deformation at joint 2 will also cause the end position $\boldsymbol{p}$ to rotate $\Delta\gamma_2$ around $\boldsymbol{K}_2$. For joint i as shown in Fig. 5(b), the end position $\boldsymbol{p}_{Ri}$ after deformation can be described as

$$\boldsymbol{P}_{Ri} = \tilde{\boldsymbol{R}}(\boldsymbol{K}_i, \Delta\gamma_i)\boldsymbol{P} \tag{1}$$

where $\boldsymbol{P}$ and $\boldsymbol{P}_{Ri}$ are homogeneous form with $\boldsymbol{P} = (\boldsymbol{p}, 1)^{\mathrm{T}}$ and $\boldsymbol{P}_{Ri} = (\boldsymbol{p}_{Ri}, 1)^{\mathrm{T}}$, respectively. $\tilde{\boldsymbol{R}}(\boldsymbol{K}_i, \Delta\gamma_i)$ represents a rotational transformation with rotating $\Delta\gamma_i$ around $\boldsymbol{K}_i$, and it is defined as follows:

$$\tilde{\boldsymbol{R}}(\boldsymbol{K}_i, \Delta\gamma_i) = \begin{bmatrix} \boldsymbol{R}(\boldsymbol{K}_i, \Delta\gamma_i)_{3\times 3} & \boldsymbol{O}_{3\times 1} \\ \boldsymbol{O}_{1\times 3} & 1 \end{bmatrix}$$
$$\boldsymbol{R}(\boldsymbol{K}_i, \Delta\gamma_i) = c\Delta\gamma_i \cdot \boldsymbol{I}_{3\times 3} + (1 - c\Delta\gamma_i) \cdot \boldsymbol{K}_i {\boldsymbol{K}_i}^{\mathrm{T}} + s\Delta\gamma_i \cdot \boldsymbol{S}(\boldsymbol{K}_i)$$
$$\boldsymbol{S}(\boldsymbol{K}_i) = \begin{bmatrix} 0 & -k_{zi} & k_{yi} \\ k_{zi} & 0 & -k_{xi} \\ -k_{yi} & k_{xi} & 0 \end{bmatrix} \tag{2}$$

where $\boldsymbol{R}(\boldsymbol{K}_i, \Delta\gamma_i)$ is the Rodigues's formula [24]. $\boldsymbol{I}_{3\times 3}$ represents an identity matrix, $\boldsymbol{O}_{1\times 3}$ is defined as $(0, 0, 0)$, and $\boldsymbol{O}_{3\times 1} = (0, 0, 0)^{\mathrm{T}}$. k_{xi}, k_{yi} and k_{zi} are three components of vector $\boldsymbol{K}_i$. $c\Delta\gamma_i$ and $s\Delta\gamma_i$ represent $\cos\Delta\gamma_i$ and $\sin\Delta\gamma_i$, respectively.

By using (1), the end position $\boldsymbol{P}_{Ri}$ after deformation at one joint can be calculated. To incorporate deformation of all joints, a recursive method is proposed. Let $\boldsymbol{P}_0$ be the end position of the robot when the joint is not deformed. The end position changes from $\boldsymbol{P}_0$ to $\boldsymbol{P}_{R1}$ after deformation at joint 1. Then, the end position changes again from $\boldsymbol{P}_{R1}$ to $\boldsymbol{P}_{R2}$ by

considering deformation at joint 2. Continue in this manner until the last joint is also considered. The process is formulated as follows

$$\begin{cases} {}^{1}\boldsymbol{P}_{\boldsymbol{R}1} = \tilde{\boldsymbol{R}}(\boldsymbol{K}_1, \Delta\gamma_1)^{1}\boldsymbol{P}_0 \\ {}^{2}\boldsymbol{P}_{\boldsymbol{R}2} = \tilde{\boldsymbol{R}}(\boldsymbol{K}_2, \Delta\gamma_2)^{2}\boldsymbol{P}_{\boldsymbol{R}1} \\ \cdots \\ {}^{i}\boldsymbol{P}_{\boldsymbol{R}i} = \tilde{\boldsymbol{R}}(\boldsymbol{K}_i, \Delta\gamma_i)^{i}\boldsymbol{P}_{\boldsymbol{R}(i-1)} \\ \cdots \\ {}^{N}\boldsymbol{P}_{\boldsymbol{R}N} = \tilde{\boldsymbol{R}}(\boldsymbol{K}_N, \Delta\gamma_N)^{N}\boldsymbol{P}_{\boldsymbol{R}(N-1)} \end{cases} \tag{3}$$

where N represents the degrees of freedom (DoF) of industrial robots. ${}^{i}\boldsymbol{P}_{\boldsymbol{R}i}$ denotes the end position after deformation by joint i. The superscript i denotes that the end position is described in the joint frame $\{i\}$. It should be noted that the rotational transformation $\tilde{\boldsymbol{R}}(\boldsymbol{K}_i, \Delta\gamma_i)$ of joint i is performed in frame $\{i\}$. The end position ${}^{i-1}\boldsymbol{P}_{\boldsymbol{R}i-1}$ after deformation by the previous joint $i-1$ is described in frame $\{i-1\}$. Therefore, ${}^{i-1}\boldsymbol{P}_{\boldsymbol{R}i-1}$ needs to be transformed into frame $\{i\}$ to perform further operations with $\tilde{\boldsymbol{R}}(\boldsymbol{K}_i, \Delta\gamma_i)$. This can be done by the homogeneous matrix ${}_{i}^{i-1}\boldsymbol{T}$ in the kinematics equation (29), i.e., ${}^{i}\boldsymbol{P}_{R(i-1)} = {}_{i-1}^{i}\boldsymbol{T}^{i-1}\boldsymbol{P}_{\boldsymbol{R}(i-1)}$ where ${}_{i-1}^{i}\boldsymbol{T} = \left({}_{i}^{i-1}\boldsymbol{T}\right)^{-1}$.

According to (3), the positioning error caused by the deformation of joint the i can be written as ${}^{i}\Delta\boldsymbol{P}_i = {}^{i}\boldsymbol{P}_{\boldsymbol{R}i} - {}^{i}\boldsymbol{P}_{\boldsymbol{R}(i-1)}$. To describe this error in frame $\{0\}$, homogeneous transformation is performed, i.e., ${}^{0}\Delta\boldsymbol{P}_i = {}_{i}^{0}\boldsymbol{T}^{i}\Delta\boldsymbol{P}_i$. Then, one can obtained that

$${}^{0}\Delta\boldsymbol{P}_i = {}_{i}^{0}\boldsymbol{T}[\tilde{\boldsymbol{R}}(K_i, \Delta\gamma_i)^{i}\boldsymbol{P}_{\boldsymbol{R}(i-1)} - {}^{i}\boldsymbol{P}_{\boldsymbol{R}(i-1)}] \tag{4}$$

Equation (4) shows that ${}^{0}\Delta\boldsymbol{P}_i$ is a nonlinear function with respect to the deformation $\Delta\gamma_i$, which is not convenient for further derivation. Since $\Delta\gamma_i$ is a small enough quantity in practice [5], [25], satisfying $\cos(\Delta\gamma_{\mathrm{i}}) \approx 1$ and $\sin(\Delta\gamma_{\mathrm{i}}) \approx \Delta\gamma_{\mathrm{i}}$, equation (2) can be simplified as

$$\boldsymbol{R}(\boldsymbol{K}_i, \Delta\gamma_i) \approx \boldsymbol{I}_{3\times3} + \boldsymbol{S}(\boldsymbol{K}_i)\cdot\Delta\gamma_i \tag{5}$$

Furthermore, $\tilde{\boldsymbol{R}}(\boldsymbol{K}_i, \Delta\gamma_i)$ in (2) can be rewritten as a first-order function with respect to $\Delta\gamma_i$ as:

$$\begin{aligned} \tilde{\boldsymbol{R}}(\boldsymbol{K}_i, \Delta\gamma_i) &= \boldsymbol{I}_{4\times4} + \begin{bmatrix} \boldsymbol{S}(\boldsymbol{K}_i) & \boldsymbol{O}_{3\times1} \\ \boldsymbol{O}_{1\times3} & 0 \end{bmatrix}\cdot\Delta\gamma_i \\ &= \boldsymbol{I}_{4\times4} + \tilde{\boldsymbol{S}}(\boldsymbol{K}_i)\cdot\Delta\gamma_i \end{aligned} \tag{6}$$

Combining (4) and (6), it can be further derived that

$${}^{0}\Delta\boldsymbol{P}_i = {}_{i}^{0}\boldsymbol{T}\tilde{\boldsymbol{S}}(\boldsymbol{K}_i)^{i}\boldsymbol{P}_{\boldsymbol{R}(i-1)}\cdot\Delta\gamma_i \tag{7}$$

According to (3), ${}^{i}\boldsymbol{P}_{\boldsymbol{R}(i-1)}$ in (7) can be recursive to ${}^{1}\boldsymbol{P}_0$, and it can be written as

$${}^{i}\boldsymbol{P}_{\boldsymbol{R}(i-1)} = \sum_{j=1}^{i-1}[{}_{j}^{i}\boldsymbol{T}\tilde{\boldsymbol{S}}(\boldsymbol{K}_j)^{j}\boldsymbol{P}_{\boldsymbol{R}(j-1)}\cdot\Delta\gamma_j] + {}_{1}^{i}\boldsymbol{T}^{1}\boldsymbol{P}_0 \tag{8}$$

By substituting (8) into (7), one can obtain that

$$\begin{aligned} {}^{0}\Delta\boldsymbol{P}_i = {}_{i}^{0}\boldsymbol{T}\tilde{\boldsymbol{S}}(\boldsymbol{K}_i)&\sum_{j=1}^{i-1}[{}_{j}^{i}\boldsymbol{T}\tilde{\boldsymbol{S}}(\boldsymbol{K}_j)^{j}\boldsymbol{P}_{\boldsymbol{R}(j-1)}\cdot\Delta\gamma_j\Delta\gamma_i] \\ &+ {}_{i}^{0}\boldsymbol{T}\tilde{\boldsymbol{S}}(\boldsymbol{K}_i){}_{1}^{i}\boldsymbol{T}^{1}\boldsymbol{P}_0\cdot\Delta\gamma_i \end{aligned} \tag{9}$$

Since the joint deformation angle $\Delta\gamma$ is within 0.0008 rad to 0.004 rad in actual industrial robots [18], the high-order term $\Delta\gamma_j\Delta\gamma_i$ can be discarded and the linear term of $\Delta\gamma$ is reserved. Then, equation (9) can be simplified as

$${}^{0}\Delta\boldsymbol{P}_i = {}_{i}^{0}\boldsymbol{T}\tilde{\boldsymbol{S}}(\boldsymbol{K}_i)^{i}\boldsymbol{P}_0\cdot\Delta\gamma_i \tag{10}$$

After reducing ${}^{0}\Delta\boldsymbol{P}_i$ from the homogeneous form to the three-dimensional vector, one can get that

$${}^{0}\Delta\boldsymbol{p}_i = {}_{i}^{0}\boldsymbol{R}\boldsymbol{S}(\boldsymbol{K}_i)^{i}\boldsymbol{p}_0\cdot\Delta\gamma_i \tag{11}$$

On the basis of (11), the total positioning error caused by the deformation of all joints is finally obtained that:

$${}^{0}\Delta\boldsymbol{p} = \sum_{i=1}^{N}{}^{0}\Delta\boldsymbol{p}_i \tag{12}$$

Equation (12) describes the relationship between deformation $\Delta\gamma_i$ around arbitrary $\boldsymbol{K}_i$-axis at joints and the positioning error ${}^{0}\Delta\boldsymbol{p}$ of industrial robots. When $\boldsymbol{K}_i = (1, 0, 0)^{\mathrm{T}}$, the mapping equation from $\Delta\gamma_x$ to the positioning error can be obtained. When $\boldsymbol{K}_i = (0, 1, 0)^{\mathrm{T}}$, the mapping equation with respect to $\Delta\gamma_y$ can be obtained. At last, the mapping relationship of $\Delta\gamma_z$ can be acquired when $\boldsymbol{K}_i = (0, 0, 1)^{\mathrm{T}}$. They will be used to establish a flexibility model in Subsection B of Section II.

B. Modelling of Flexible Deformation Error

From the analysis of Section I, three deformations occur at every joint under the payload, i.e., torsional deformation around the Z_i-axis and bending deformation around axes X_i and Y_i. According to the assumption of linear stiffness [26], three deformations at joint i can be described as follows

$$\Delta\gamma_{xi} = C_{xi}n_{xi},\ \Delta\gamma_{yi} = C_{yi}n_{yi},\ \Delta\theta_i = C_{zi}n_{zi} \tag{13}$$

where C_{xi}, C_{yi} and C_{zi} are joint flexibility coefficients. n_{xi}, n_{yi} and n_{zi} are joint applied torque in three axes, respectively. Then, through linear assumption and deformation mapping equation, a flexibility model considering all three deformations simultaneously can be established.

First, the flexibility model of the bending deformation around the X_i-axis is established. According to (11) and (13), the positioning error due to bending deformation γ_{xi} at joint i can be written as

$${}^{0}\Delta\boldsymbol{p}_{xi} = {}_{i}^{0}\boldsymbol{R}\boldsymbol{S}(\boldsymbol{K}_{xi})^{i}\boldsymbol{p}_0\cdot C_{xi}n_{xi} \tag{14}$$

where $\boldsymbol{K}_{xi} = (1, 0, 0)^{\mathrm{T}}$. Furthermore, by adding the part of each joint, the total error can be obtained as

$${}^{0}\Delta\boldsymbol{p}_x = \sum_{i=1}^{N}{}_{i}^{0}\boldsymbol{R}\boldsymbol{S}(\boldsymbol{K}_{xi})^{i}\boldsymbol{p}_0\cdot C_{xi}n_{xi} \tag{15}$$

By reforming (25), the flexibility model describing the error caused by bending deformation around the X-axis under the applied torque $\boldsymbol{n}_x$ can be derived as

$${}^{0}\Delta\boldsymbol{p}_x = \boldsymbol{J}_{\gamma x}\boldsymbol{\Lambda}(\boldsymbol{n}_x)\boldsymbol{C}_x \tag{16}$$

where $\boldsymbol{J}_x = \left[{}_{1}^{0}\boldsymbol{R}\boldsymbol{S}(\boldsymbol{K}_{x1})^{1}\boldsymbol{p}_0 \cdots {}_{N}^{0}\boldsymbol{R}\boldsymbol{S}(\boldsymbol{K}_{xN})^{N}\boldsymbol{p}_0\right]$ is defined as the Jacobian matrix with regard to $\Delta\gamma_x$. The diagonal matrix is $\boldsymbol{\Lambda}(\boldsymbol{n}_x) = diag(n_{x1}, \cdots, n_{xi}, \cdots n_{xN})$, and the flexibility coefficient vector is $\boldsymbol{C}_x = (C_{x1}, C_{x2}, \cdots, C_{xN})^{\mathrm{T}}$.

Second, the flexibility model of the bending deformation around the Y_i-axis can be obtained by means of (11), (12) and (13). The positioning error equation is written as

$$^0\Delta \boldsymbol{p}_y = \sum_{i=1}^{N} {}^0_i\boldsymbol{RS}(\boldsymbol{K}_{yi})^i\boldsymbol{p}_0 \cdot C_{yi}n_{yi} \tag{17}$$

$$^0\Delta \boldsymbol{p}_z = \sum_{i=1}^{N} {}^0_i\boldsymbol{RS}(\boldsymbol{K}_{zi})^i\boldsymbol{p}_0 \cdot C_{zi}n_{zi} \tag{18}$$

where $\boldsymbol{K}_{yi} = (0, 1, 0)^{\mathrm{T}}$.

For simplicity, equation (17) can be rewritten as

$$^0\Delta \boldsymbol{p}_y = \boldsymbol{J}_{\gamma y}\boldsymbol{\Lambda}(\boldsymbol{n}_y)\boldsymbol{C}_y \tag{19}$$

where $\boldsymbol{J}_{\gamma y} = \left[{}^0_1\boldsymbol{RS}(\boldsymbol{K}_{y1})^1\boldsymbol{p}_0 \cdots {}^0_N\boldsymbol{RS}(\boldsymbol{K}_{yN})^N\boldsymbol{p}_0\right]$ is a Jacobian matrix related to the bending deformation γ_{yi}. $\boldsymbol{\Lambda}(\boldsymbol{n}_y) = diag(n_{y1}, \cdots, n_{yi}, \cdots n_{yN})$ is diagonal matrix, and $\boldsymbol{C}_y = (C_{y1}, C_{y2}, \cdots, C_{yN})^{\mathrm{T}}$ denotes a vector of flexibility coefficients of the Y-axis.

Third, the flexibility model of the torsional deformation around the Z_i-axis is built. By using (11), (12) and (13), the equation with the same form as (16) and (19) can be obtained

$$^0\Delta \boldsymbol{p}_z = \boldsymbol{J}_{\gamma z}\boldsymbol{\Lambda}(\boldsymbol{n}_z)\boldsymbol{C}_z \tag{20}$$

where the meanings of each sign are similar to before those given, except for $\boldsymbol{K}_{zi} = (0, 0, 1)^{\mathrm{T}}$. Finally, a flexibility model incorporating three deformations can be derived by adding up $^0\Delta \boldsymbol{p}_x$, $^0\Delta \boldsymbol{p}_y$ and $^0\Delta \boldsymbol{p}_z$, i.e., $^0\Delta \boldsymbol{p} = {}^0\Delta \boldsymbol{p}_x + {}^0\Delta \boldsymbol{p}_y + {}^0\Delta \boldsymbol{p}_z$, and one can get that

$$^0\Delta \boldsymbol{p} = \left[\boldsymbol{J}_x\boldsymbol{\Lambda}(\boldsymbol{n}_x)\ \boldsymbol{J}_y\boldsymbol{\Lambda}(\boldsymbol{n}_y)\ \boldsymbol{J}_z\boldsymbol{\Lambda}(\boldsymbol{n}_z)\right]\begin{bmatrix}\boldsymbol{C}_x\\ \boldsymbol{C}_y\\ \boldsymbol{C}_z\end{bmatrix} \tag{21}$$

Equation (20) is the proposed flexibility model, which characterizes the relationship between the joint applied torque and the positioning error. Since the dominant factors are incorporated, its predicted accuracy can be guaranteed. The proposed model only includes $3N$ parameters where N denotes the number of robot's degrees of freedom, while the conventional 6-DoF model has $36N$ parameters ($\bar{\boldsymbol{C}}_i \in \mathbb{R}^{6\times 6}$ shown in Model III of Appendix III) [18], and $18N$ parameters ($\bar{\boldsymbol{C}}_i \in \mathbb{R}^{6\times 3}$) even without considering the posture error. The complexity of the proposed model is reduced, which is convenient for practical applications. On the other hand, the proposed model provides more favorable conditions for parameter identification shown in Subsection C of Section II. In addition, some discussions on (20) are given that:

1) When the joint flexibility properties of the robot in X, Y and Z directions are different, there are three flexible coefficients for each joint, i.e., $\boldsymbol{C}_x$, $\boldsymbol{C}_y$ and $\boldsymbol{C}_z$. The positioning error caused by joint deformation is described by (21).
2) When the joint flexibility properties in X and Y directions are similar, it can be argued that $\boldsymbol{C}_x \approx \boldsymbol{C}_y = \boldsymbol{C}_r$. Equation (21) is degenerated as

$$^0\Delta \boldsymbol{p} = \left[\boldsymbol{J}_x\boldsymbol{\Lambda}(\boldsymbol{n}_x) + \boldsymbol{J}_y\boldsymbol{\Lambda}(\boldsymbol{n}_y)\ \boldsymbol{J}_z\boldsymbol{\Lambda}(\boldsymbol{n}_z)\right]\begin{bmatrix}\boldsymbol{C}_r\\ \boldsymbol{C}_z\end{bmatrix} \tag{22}$$

This indicates that the joint property is determined by the radial flexibility $\boldsymbol{C}_r$ and axial flexibility $\boldsymbol{C}_z$, which has been involved in our previous work [27].
3) When the axial flexibility is much greater than the non-axis flexibility, i.e., $\boldsymbol{C}_r \ll \boldsymbol{C}_z$, the joint flexibility will be determined by the axial flexibility $\boldsymbol{C}_z$, while the non-axis flexibility $\boldsymbol{C}_r$ can be ignored. Equation (21) will be further degenerated as (20).

C. Identification Method for Flexibility Coefficient

For simplicity, let equation (21) be written as

$$^0\Delta \boldsymbol{p} = \boldsymbol{HC} \tag{23}$$

where $\boldsymbol{H} = \left[\boldsymbol{J}_x\boldsymbol{\Lambda}(\boldsymbol{n}_x)\ \boldsymbol{J}_y\boldsymbol{\Lambda}(\boldsymbol{n}_y)\ \boldsymbol{J}_z\boldsymbol{\Lambda}(\boldsymbol{n}_z)\right]$, and $\boldsymbol{C} = (\boldsymbol{C}_x, \boldsymbol{C}_y, \boldsymbol{C}_z)^{\mathrm{T}}$. In (23), the flexibility coefficient $\boldsymbol{C}$ is linear with respect to the positioning error $^0\Delta \boldsymbol{p}$. The flexibility coefficient $\boldsymbol{C}$ can be identified by the least squares method [28]. The data of M different joint torques are estimated and configurations need to be collected, requiring $M > N$. Joint applied torques can be estimated by the algorithms as [29] or obtained by the robot's controller. There is one equation for each data, i.e., $^0\Delta \boldsymbol{p}_{(i)} = \boldsymbol{H}_{(i)}\boldsymbol{C}$. For M groups of data, an overdetermined system of equations can be obtained as

$$\begin{bmatrix} ^0\Delta \boldsymbol{p}_{(1)} \\ ^0\Delta \boldsymbol{p}_{(2)} \\ \vdots \\ ^0\Delta \boldsymbol{p}_{(M)} \end{bmatrix} = \begin{bmatrix} \boldsymbol{H}_{(1)} \\ \boldsymbol{H}_{(2)} \\ \vdots \\ \boldsymbol{H}_{(M)} \end{bmatrix}\boldsymbol{C}$$
$$\boldsymbol{Y} = \boldsymbol{\Phi C} \tag{24}$$

Through the least squares method, the estimated value $\hat{\boldsymbol{C}}$ of the flexibility coefficient is calculated by

$$\hat{\boldsymbol{C}} = (\boldsymbol{\Phi}^{\mathrm{T}}\boldsymbol{\Phi})^{-\Delta}\boldsymbol{\Phi}^{\mathrm{T}}\boldsymbol{Y} \tag{25}$$

From (25), the flexibility coefficient can be readily identified without multiple iterations or using the FEMs as in conventional methods, which makes the proposed model simple to implement in practical applications.

IV. Experiments and Results

A. Experimental Setup

To examine the effectiveness of the established flexibility model (21), an experimental setup is constructed as shown in Fig. 6, which consists of a measuring equipment, two data collection software developed based on Qt 5.12 (64-bit), a 6-DoF serial robot and a set of payloads. The measuring equipment includes an R-20 Radian laser tracker and a 1.5" Spherical Mounted Retro-reflector(SMR). The R-20 Radian laser tracker is used to measure the end position of the robot, and its measuring accuracy is 10 μm+5 μm/m. SMR receives and reflects a laser beam to the laser tracker. The 6-DoF serial robot used in the experiment is an ELITE-EC66 robot, and the repeated accuracy is 0.03 mm. The applied torque of each joint and the joint angle can be collected from the controller in real-time. Its working radius is 914 mm, and the maximum payload is 6 kg. The payloads consist of two 0.5 kg, two 1 kg and two 2 kg weights, which are used to compose variable



Fig. 6. Experimental setup.

TABLE II
THE IDENTIFIED FLEXIBILITY COEFFICIENTS OF EACH JOINT

Number	C_{xi} (rad/Nm)	C_{yi} (rad/Nm)	C_{zi} (rad/Nm)
Joint 1	6.97×10^{-6}	9.61×10^{-4}	8.32×10^{-5}
Joint 2	7.31×10^{-6}	8.71×10^{-6}	1.15×10^{-3}
Joint 3	5.63×10^{-5}	4.62×10^{-5}	5.86×10^{-5}
Joint 4	1.78×10^{-4}	7.61×10^{-4}	2.81×10^{-5}
Joint 5	3.77×10^{-5}	5.32×10^{-3}	1.27×10^{-3}
Joint 6	4.64×10^{-4}	3.49×10^{-4}	0

payloads of 0.5 kg to 4.5 kg. The function of the flange plate installed at the end of the robot is to fix SMR and suspend weights.

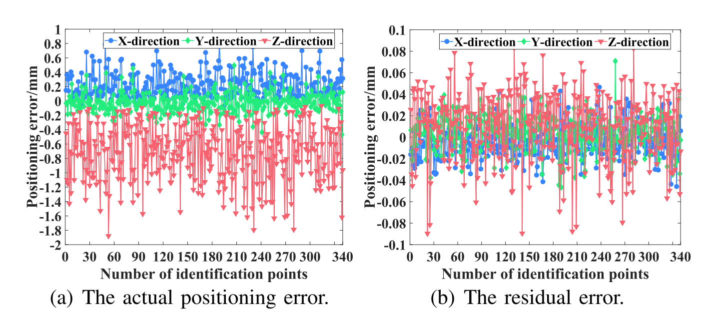
B. Identification of Flexibility Coefficients

According to (24) and (25), flexibility coefficients of all joints can be identified. In workspace of the robot, 54 different configurations are selected randomly. The robot moves at these configurations one by one, and its end position is measured by the laser tracker. The joint applied torque and joint angle are provided by the robot controller. The experiment is performed under 9 payloads including, 0.5 kg, 1 kg, 1.5 kg, 2 kg, 2.5 kg, 3 kg, 3.5 kg, 4 kg and 4.5 kg. The total amount of data is $54 \times 9 = 486$ where 340 groups of data are selected as identification data, and the remaining 146 groups of data are used as the validation data. The positioning error ${}^0\Delta \boldsymbol{p}_{(i)}$ in (24) is calculated by subtracting the measured position of no payloads from that of payloads. The regression matrix $\boldsymbol{H}_{(i)}$ is calculated by the joint applied torque and joint angle. Then, flexibility coefficients of all joints can be identified as shown in Table II.

In Table II, all other parameters are obtained except for C_{z6}. The main reason is that the line of action of the payload approximately passes through the origin of frame {6}. The payload does not cause flexible deformation around the axis of joint 6. Thus, C_{z6} cannot be identified here. If the end flange is allowed to apply a payload deviating from frame {6}, then the flexibility coefficient C_{z6} can be identified. Furthermore, to examine the effectiveness of identification results, a residual error index is defined as follows

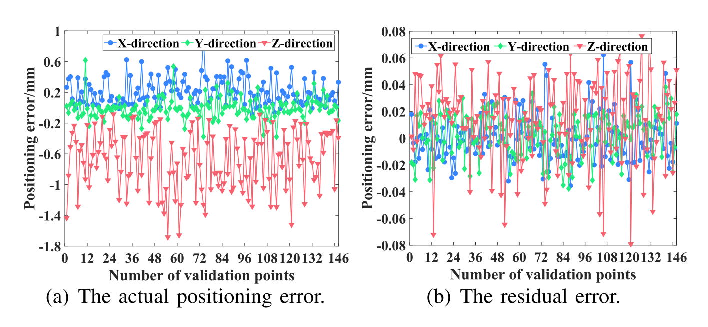
$$\boldsymbol{e}_r = {}^0\Delta \boldsymbol{p}^a - {}^0\Delta \boldsymbol{p}^c \tag{26}$$

where ${}^0\Delta \boldsymbol{p}^a$ denotes the actual positioning error via measuring, and ${}^0\Delta \boldsymbol{p}^c$ is the predicted positioning error by (21).



(a) The actual positioning error. (b) The residual error.

Fig. 7. Comparison of the actual and residual error in identification data.



(a) The actual positioning error. (b) The residual error.

Fig. 8. Comparison of the actual and residual error in validation data.

The effectiveness of the identification result can be determined by comparing $\boldsymbol{e}_r$ and ${}^0\Delta \boldsymbol{p}^a$. When $\|\boldsymbol{e}_r\|_2 < \left\|{}^0\Delta \boldsymbol{p}^a\right\|_2$, the identification result is valid. The closer the residual error $\boldsymbol{e}_r$ is to 0, the more accurate the model is. Fig. 7 shows the actual positioning error ${}^0\Delta \boldsymbol{p}^a$ caused by payloads on the identification data. According to the identified coefficients in Table II and (21), the predicted positioning error ${}^0\Delta \boldsymbol{p}^c$ is calculated, and the residual error $\boldsymbol{e}_r$ is calculated as shown in Fig. 7(b). Compared with the actual positioning error, the range of the residual error $\boldsymbol{e}_r$ is narrowed to [-0.1 mm, 0.1 mm] accounting for 10%, which indicates that the identified coefficients are valid on the identification data. Similarly, the identification result is verified on the validation data. The actual positioning error of the validation data is shown in Fig. 8(a), and the corresponding residual error is calculated as shown in Fig. 8(b). The residual error of the validation data is within 0.08 mm, which only accounts for 8% of the actual positioning error. In light of $\boldsymbol{e}_r$ of both identification and validation data, the identified flexibility coefficients are effective. It also shows that the proposed flexibility model and its identification method are valid.

C. Performance Evaluation of the Proposed Model

The performance evaluation of the proposed flexibility model (21) is conducted from three aspects including prediction accuracy, accuracy stability and applicability. Since the proposed model considers major rotational deformations by removing translational deformations, its accuracy theoretically is lower than that of the model including six directions

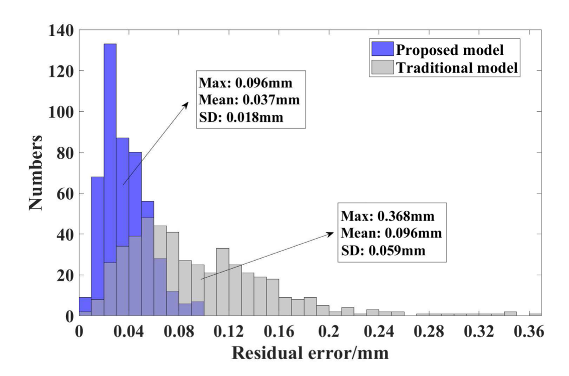


Fig. 9. Statistical histograms of residual error for the proposed model and Model I.

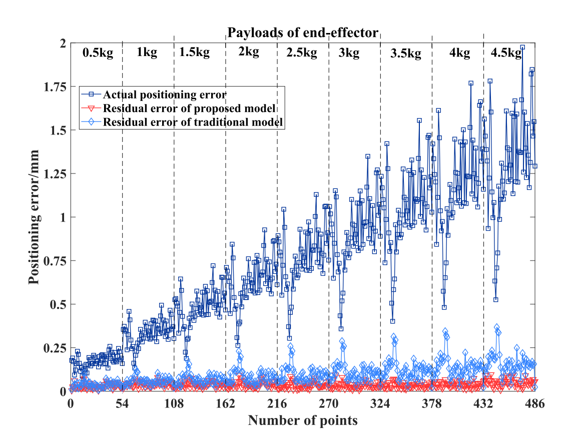


Fig. 10. The variation of three errors with increasing payloads.

deformation. In respect to accuracy performance, this paper mainly compares the proposed model with the 1-DoF model (called Model I) [7] that has been most widely used until now. To analyze the prediction accuracy of these two models, the 2-norm $\|\boldsymbol{e}_r\|_2$ of residual errors is calculated, and statistical histograms are obtained as shown in Fig. 9 where each histogram covers 0.01mm. The results show that residual error distribution of the proposed model is more concentrated with a smaller maximum and mean. The proposed model's maximum, mean and standard deviation decreases 73.81%, 61.15% and 69.70% versus the traditional model, respectively. The prediction accuracy λ of the traditional model and proposed model is calculated by (27) as 81.12% and 95.63%, respectively. Thus, the proposed model describes deformation error more accurately than the traditional model, which is consistent the analysis results in Section II.

$$\lambda = (1 - \max \|\boldsymbol{e}_r\|_2 / \max \left\|{}^0\Delta \boldsymbol{p}^a\right\|_2) \times 100\% \tag{27}$$

Furthermore, the stability of prediction accuracy for the proposed model is analyzed with the payload increasing. The variation of three errors, i.e., the actual positioning error, the residual error of the traditional model, and the residual error of the proposed model, with increasing payloads is shown in Fig. 10. With an increase in payloads, the actual positioning error is increased quickly. The residual error calculated by the traditional model increase also as payloads increase, while the residual error obtained by the proposed model does not clearly change with increasing payloads. This initially indicates that the proposed model has higher stability in accuracy when the load increases compared with the traditional model. To quantify the stability of prediction accuracy, an index based on the average residual error of each payload is defined as

$$\xi = (M_{\max} - M_{\min})/M_{\min} \tag{28}$$

where $M_{\max}$ and $M_{\min}$ represent the maximum and minimum value of the average residual error among all payloads. The average residual error of each payload is calculated as shown Table III. According to Table III and (28), the stability index of traditional and proposed model can be calculated as $\xi_B = 2.99$ and $\xi_P = 0.70$, respectively. This indicates that amount of change in the residual error of the traditional model exceeds that of the proposed model by more than 4 times. Therefore, the prediction accuracy of the proposed model is more stable than that of the traditional model.

TABLE III
THE IDENTIFIED FLEXIBILITY COEFFICIENTS OF EACH JOINT

	0.5kg	1kg	1.5kg	2kg	2.5kg	3kg	3.5kg	4kg	4.5kg
M_T	0.038	0.058	0.068	0.082	0.093	0.108	0.121	0.138	0.167
M_P	0.030	0.041	0.039	0.039	0.034	0.033	0.033	0.037	0.051

M_T and M_P represent the average residual error obtained by the traditional and proposed model, respectively. The unit is mm.

TABLE IV
COMPARISON OF MODEL'S PARAMETERS AND COMPLEXITY

	Model I	Model II	Model III	Proposed model
Number of parameters	N	$N + 36(N + 1)$	$36N$	$3N$
o	$6N^2 + 15N + 6$	$6N^2 + 312N + 318$	$1650N + 924$	$18N^2 - 3$

The symbol N denotes the robot's degrees of freedom (DoF).

In addition to the above aspects, the applicability of the flexibility model is also a concerned issue in practical engineering. To quantify the computational cost, the complexity of the proposed model and traditional models is compared. Since the flexibility model mainly involves matrix multiplication operations, the complexity o is defined as the sum of the addition and multiplication times of matrix operations. According to the proposed model (21) and the traditional Model I (35) [7], Model II (36) [17], and Model III (37) [18] in Appendix III, the complexity o can be calculated and shown in Table IV. Then, the computational complexity of flexibility models as the number of robot's degrees of freedom increases is shown in Fig. 11. The proposed model has lower computational complexity compared to traditional 6-DoF Models II and III.

In applications, for an industrial computer with a central processing unit (CPU) frequency of 2.5 GHz (one clock cycle: 0.4 ns), its each multiplication operation takes 5 clock cycles. According to the complexity o in Table IV, the computational requirements for one error prediction can be assessed as shown in Table V. The proposed model requires only 1.290 ms, while 6-DoF Models II and III require 4.812 ms and 21.648 ms, respectively. The 1-DoF Model I takes the least amount of time 0.624 ms, but it has low prediction accuracy. For parameter identification, the flexibility coefficients of the proposed model can be conveniently identified by the least squares method as in Model I. In contrast, the parameter identification of Model II requires the use of FEMs. Similarly, this method is used for

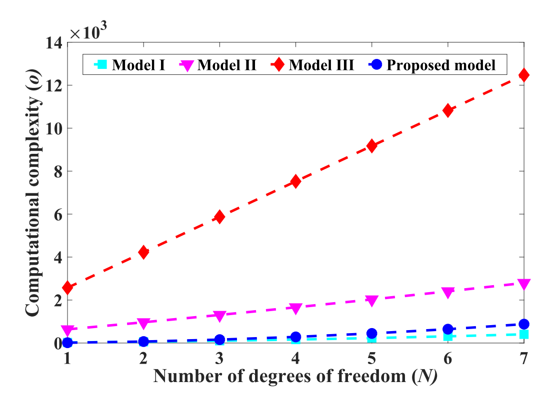


Fig. 11. The computational cost scale of flexibility models with the number of degrees of freedom.

TABLE V
COMPARISON OF PERFORMANCE AMONG FLEXIBILITY MODELS

	Model I [7]	Model II [17]	Model III [18]	Proposed model
Prediction accuracy	81.4%	92.1%	94.5%	95.1%
Accuracy stability	2.99	-	-	0.70
Number of parameters	6	222	258/26	18
Time cost (ms)	0.624	4.812	21.648	1.290

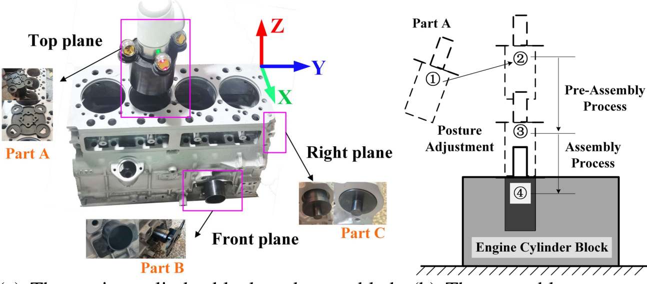
Symbols "-" denote that the corresponding index cannot be calculated according to author's data. "258/26" represents that the original number of parameters in the model is 258, and it is 26 after reducing by the author.

Model III before simplification. Although the parameters of Model III can be simplified, they require the use of 19 complex rules in sequence. These make it difficult to apply Model II and Model III in practical engineering. Therefore, in contrast, the proposed model has good applicability.

Based on evaluation analysis, the performance comparison of the proposed model with other models is summarized as shown in Table V. As a whole, the proposed model is more accurate and stable than Model I (1-DoF model) to predict the deformation error of industrial robots. Meanwhile, the complexity of the proposed model is reduced compared with Model II and Model III (6-DoF model), achieving the main purpose of this paper.

D. Compensation for Flexible Error in Assembly Task

In this section, the proposed model is used to compensate for the pose (posture and position) error caused by the flexible deformation of the Elite EC66 robot in three assembly tasks. As shown in Fig. 12(a), there are three parts in an engine cylinder block of automations, including part A, part B and part C, which need to be assembled by the robot. Their masses are 3.5kg, 2.7kg and 1.5kg respectively. Part A is assembled into the cylinder chamber on the top plane of the engine along the negative direction of the Z-axis. Parts B and C are assembled into the front and right installation holes along the negative direction of the X-axis and Y-axis, respectively. To achieve this, the robot needs to work in three different configurations. Each assembly operation includes three processes, as shown in Fig. 12(b). In the first process, the robot moves from a certain starting position ① to the pre-assembly position ② and completes the adjustment of the assembly posture. Then, the robot moves from position ② to



(a) The engine cylinder block and assembled parts. (b) The assembly process.

Fig. 12. The assembly of automotive engine parts.

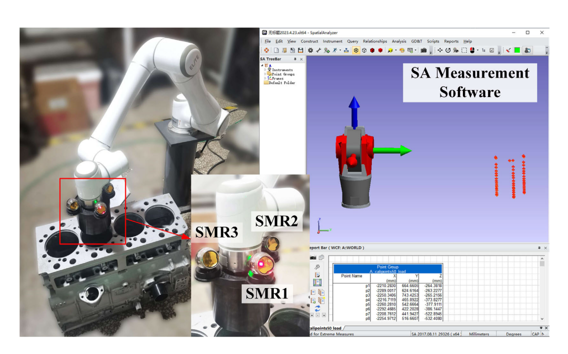
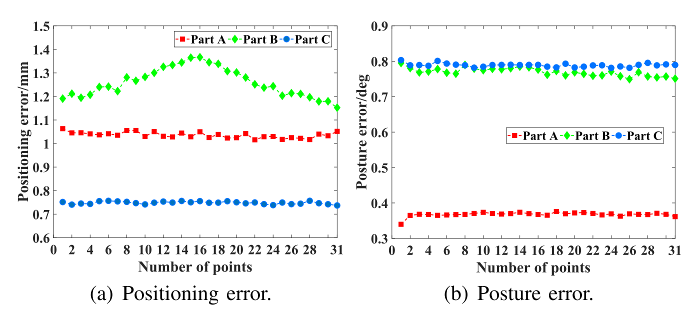


Fig. 13. The measurement of pose by the laser tracker during the assembly process.

the assembly position ③ and the posture is adjusted slightly, called the pre-assembly process. The last is assembly process. The robot moves to the full assembly position ④ from position ③ and the posture does not change during this process. The compensation for flexible errors is mainly performed during the pre-assembly and assembly processes, as these two processes directly determine the safety and accuracy of assembly tasks. According to the fit tolerance of parts, the pose error of the end-effector during assembly operation must be within 0.2mm and 0.03° to guarantee that the assembled parts will not be damaged due to collision. To monitor the pose error of the robot during the assembly process, the coordinates of three SMRs (SMR1, SMR2 and SMR3) are measured by the laser tracker. As shown in Fig. 13, three SMRs are fixed on the end-effector of the robot. During measurement, the coordinates of SMR1, SMR2 and SMR3 are collected in sequence at each assembly position. According to the measured coordinates, the pose can be calculated, and the pose error can also be obtained.

According to the assembly process in Fig. 12(b), parts A, B and C are assembled into the engine cylinder block by programming the robot, respectively. Under the payload of assembly parts, there is an error between the desired and actual pose due to the flexible deformation of the joint. To avoid damaging parts and the cylinder block, the pose error caused by flexible deformation needs to be measured before assembly. For each part, 31 positions in the assembly path are selected as measured points. By measuring the coordinates with and without payloads, the pose error can be obtained, as shown in Fig. 14. The maximum position error of parts A, B and C is 1.063mm, 1.366mm and 0.756mm, respectively. The maximum posture error of the three parts is 0.376°, 0.795° and 0.788°, respectively. Since the pose error for assembly tasks



(a) Positioning error. (b) Posture error.

Fig. 14. The positioning and posture error of part A, part B and part C before compensation.

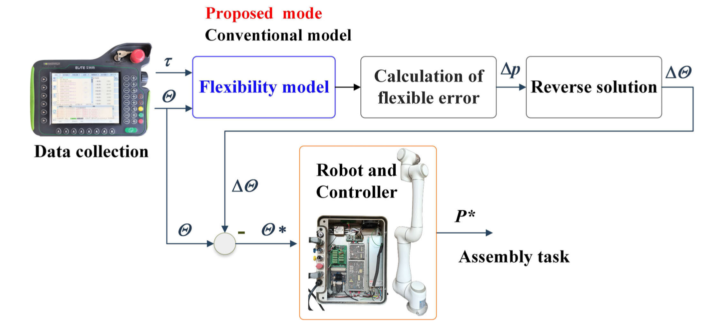
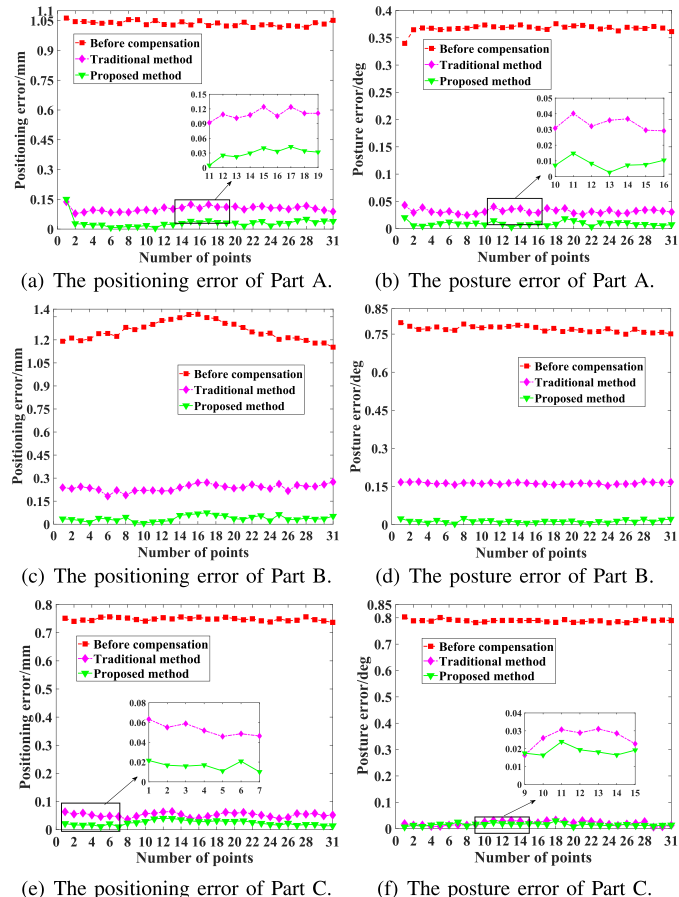


Fig. 15. The block diagram of error compensation.

must be less than 0.2mm and 0.03°, the assembly of all three parts cannot be completed. If an assembly operation is performed in this situation, the parts and engine casing will be damaged.

To reduce the pose error during assembly tasks, a compensation method (reference to Appendix II for details) for flexible errors is designed as shown in Fig. 15. Firstly, the joint applied torque $\boldsymbol{n}$ and the joint angle $\boldsymbol{\Theta}$ are collected from the robot. The sign $\boldsymbol{\Theta} = (\theta_1, \theta_2, \theta_3, \theta_4, \theta_5, \theta_6)^{\mathrm{T}}$ represents joint angles for the six joints of the robot, where θ_i denotes the joint angle of the joint i. Then, the positioning error $\Delta \boldsymbol{p}$ can be calculated by the flexibility model. Inverse kinematics is introduced to transform the positioning error $\Delta \boldsymbol{p}$ to the corresponding angular error $\Delta \boldsymbol{\Theta}$. Finally, by compensating $\Delta \boldsymbol{p}$ to $\boldsymbol{\Theta}$, a new joint angle $\boldsymbol{\Theta}^* = \boldsymbol{\Theta} - \Delta \boldsymbol{\Theta}$ can be obtained and is used to drive the robot. The pose accuracy of the robot can be improved by this approach. The compensation effect is determined by the accuracy of the flexibility model.

Based on the method in Fig. 15, the compensation for the flexible error is performed by the traditional and proposed models. The results of error compensation is shown in Fig. 16. Among three assembly tasks, the pose error is reduced after compensation by the traditional model. Compared with the results before compensation, the pose accuracy of the robot has been significantly improved. The results indicate that the compensation accuracy of the traditional model is not stable. When the mass of the assembled part is small and the robot is in the constricted configuration, the compensation accuracy is better, as shown in Fig. 16(e) and Fig. 16(f). On the contrary, the compensation accuracy will become worse when the mass increases and the robot is in the extended configuration, as shown in Fig. 16(c) and Fig. 16(d). The main reason is that only the rotational deformation around the joint axis can be predicted and compensated in the traditional model. In some configurations, such as extended configurations, the rotational deformation error around the non-axis of the joint accounts for a larger proportion of the total error. This component will also increase as the payload increases, but the traditional model cannot address it. In the proposed model, the bending deformations of the joint around the X and Y-axes are considered in addition to the torsional deformation about the Z-axis, which has highly predicted accuracy for the flexible error. After compensation by the proposed model, the pose error in the assembly path is further reduced verse the traditional method. For three assembly tasks, there is no significant fluctuation in the pose accuracy, which is within 0.1mm and 0.03°.



(a) The positioning error of Part A. (b) The posture error of Part A.

(c) The positioning error of Part B. (d) The posture error of Part B.

(e) The positioning error of Part C. (f) The posture error of Part C.

Fig. 16. The positioning and posture error of parts on three planes after compensation by the traditional model and proposed model.

The detailed statistical results are shown in Table VI by analyzing the maximum value, mean value, and standard deviation of the pose error. Before compensation, the maximum pose error corresponding to three assembly tasks is 1.063mm/0.376°, 1.366mm/0.795° and 0.756mm/0.803°, respectively, which does not satisfy the requirements. After compensation by the traditional model, the positioning errors for parts A and C satisfy the assembly requirements, but their posture errors are not sufficient. For part B, both positioning and posture errors cannot satisfy the requirements. After compensation by the proposed model, the maximum pose error of part A is reduced from 0.124mm/0.043° to 0.05mm/0.02°, and compensation accuracy improves by 59.67% and 53.48%,

TABLE VI
STATISTICAL RESULTS OF POSITIONING AND POSTURE ERROR IN THREE ASSEMBLY SITUATIONS BEFORE AND AFTER ERROR COMPENSATION

		Positioning error /mm			Posture error /°		
		Maximum value	Mean value	Standard deviation	Maximum value	Mean value	Standard deviation
Part A	Before compensation	1.063	1.036	0.012	0.376	0.368	0.006
	Traditional method	0.124	0.102	0.012	0.043	0.032	0.004
	Proposed method	**0.050**	**0.027**	0.012	**0.020**	**0.009**	0.004
Part B	Before compensation	1.366	1.258	0.061	0.795	0.769	0.011
	Traditional method	0.274	0.237	0.022	0.171	0.163	0.003
	Proposed method	**0.075**	**0.038**	**0.018**	**0.025**	**0.013**	0.005
Part C	Before compensation	0.756	0.748	0.006	0.803	0.788	0.005
	Traditional method	0.064	0.052	0.008	0.033	0.020	0.008
	Proposed method	**0.040**	**0.023**	0.008	**0.029**	**0.015**	**0.005**

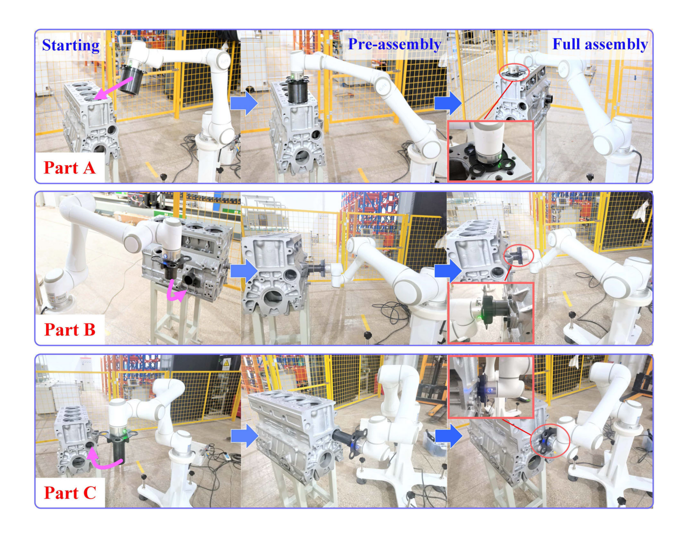


Fig. 17. The actual assembly of three parts after error compensation.

respectively. For part B, the maximum pose error is reduced from 0.274mm/0.171° to 0.075mm/0.025°, and compensation accuracy improves by 72.62% and 85.38%, respectively. And then, the maximum pose error of part C is reduced from 0.064mm/0.033° to 0.040mm/0.029°. Its compensation accuracy improves by 37.5% and 12.21%, respectively. Finally, the path after error compensation is used to achieve a high-precision assembly of the part as shown in Fig. 17.

E. Discussion for Results

The experimental results demonstrate that the proposed flexibility model surpasses traditional 1-DoF flexibility models in accuracy performance and is more preferable over conventional 6-DoF models in applicability, in line with the expectations of this study. However, there are several results that are noteworthy. The first is accuracy results of several models in Table V. The proposed model has a higher prediction accuracy than Model I, which is reasonable because flexible deformations in the X and Y-axes are incorporated. Nevertheless, the result that the proposed model has higher prediction accuracy than Models II and III is not intuitive. Since Models II and III theoretically include additional translational deformation at the joints than the proposed model, the accuracy of the proposed model should be slightly lower than that of Models II and III. The possible reason for this is that Models II and III do not consider the effect of supplementary flexibility [9], [13], and the supplementary flexibility increases with the payload. The experimental results of Models II and III were obtained on a robot with a large payload of more than 200 kg, while the results of this paper were obtained on a robot with a small payload of 6 kg. The accuracy of Models II and III is lower than the accuracy of the proposed model due to the deformation caused by the supplementary flexibility. Therefore, the effect of supplementary flexibility can be further considered to maintain the high accuracy of the proposed model for large-payload robots.

The second is the compensation results for the assembly task. Overall, the proposed models have better compensation results than Model I, which is consistent with the theoretical analysis. However, in Fig. 16, the proposed model in some configurations (e.g., for part B) shows a more significant advantage over Model I, while in other configurations their results are comparable (e.g., for part C). This indicates that the three flexibility factors at the joint do not affect the positioning error in all configurations. In some configurations, some of the flexibility factors may not work. Therefore, the flexibility model can be simplified (reference to the end of part B) to reduce the computational effort without affecting its accuracy performance. By proposing a new judgment index to determine which model to use in which configuration, it will help to improve the efficiency of flexible deformation error compensation in real systems. However, how to construct this reasonable judgment indicator is still an open question.

Some limitations of this study are that: the linear flexibility assumption employed in the proposed model may restrict the prediction accuracy for the robot with strongly nonlinear flexibility. The model can be enhanced by incorporating nonlinear flexibility models, such as cubic polynomials, quantic polynomials or arc tangent models [30]. Then, for the consideration of model lightweight, all nonlinear characteristics at joints, such as hysteresis, backlash and drift [31], are neglected, which may result in inaccurate parameter identification when these factors have a significant impact. It can be addressed by considering these nonlinear characteristics to increase its accuracy. In experiments, the proposed model has been validated on

small-payload robots with harmonic drive joints. To generalize the model, further validation on other robots is needed as well, such as large-payload robots with RV reducer joints and heavy-duty robots with a stiffness compensator.

In summary, the proposed flexibility error model can describe the relationship between payloads and positioning errors more accurately than traditional models. Moreover, the proposed model has a more stable ability to characterize flexible deformation errors when the robot's payload increases. The proposed model can be directly applied to compensate for positioning errors in high-precision applications [32], [33], [34], such as robotic machining, robotic assembly and multi-robot collaboration. Then, the proposed model can be further converted into a Cartesian flexibility model. By optimizing the robot's pose, a workspace with better stiffness performance can be obtained. Finally, the proposed model can also be combined with existing neural network-based compensation methods to construct a more complete flexibility model for nonlinear characteristics at joints.

V. Conclusion

Through analyzing critical factors affecting the positioning error of robots, this paper proposes a high-accuracy flexibility model of joints that can be implemented in practical applications. Parameter identification and error compensation are performed on a 6-DoF industrial robot. The main conclusions can be summarized as follows. 1) Rotational deformation at the joints is the dominant factor resulting in the robot positioning error, contributing more than 90% of the positioning error. 2) Compared with the most widely used 1-DoF models, the proposed model improves the prediction accuracy by 13.70% and the accuracy stability by 4.27 times. 3) In contrast to the 6-DoF model with 200 parameters, the proposed model is reduced to 18 parameters, which decreases the difficulty of parameter identification. 4) After compensation by the proposed model, the pose accuracy of the three assembled parts is improved, with the maximum improvement of 72.62% and 85.38%. In summary, the proposed flexibility model is effective. Compared with traditional models, the proposed model combines both high accuracy performance and applicability. Future work will further improve the proposed model and apply it to the on-line compensation of flexible deformation errors.

Appendix A
Positioning Error Model for Contribution Analysis

As shown in Fig. 1(a), the rigid kinematics equation can be described by the MD-H coordinate transformation [35] as

$$\boldsymbol{T} = \prod_{i=1}^{N}\left[{}_{i}^{i-1}\boldsymbol{T}(\theta_i)\right]{}_{E}^{N}\boldsymbol{T} = \begin{bmatrix} \boldsymbol{R}_{3\times 3} & \boldsymbol{P}_{3\times 1} \\ \boldsymbol{O}_{1\times 3} & 1 \end{bmatrix} \tag{29}$$

where N is the number of robot's joint. ${}_{i}^{i-1}\boldsymbol{T}$ denotes a homogeneous transform matrix between frame $\{i-1\}$ and frame $\{i\}$. ${}_{E}^{N}\boldsymbol{T}$ represents a transform matrix from frame $\{N\}$ to end-effector frame $\{E\}$. θ_i is a joint angle. $\boldsymbol{R}$ and $\boldsymbol{P}$ denote the posture and position of the end-effector, respectively. $\boldsymbol{O} = (0, 0, 0)^{\mathrm{T}}$.

Considering virtual springs as shown in Fig. 1(b), the deformed kinematics equation can be described as

$$\boldsymbol{T}' = \prod_{i=1}^{N}\left[{}_{i}^{i-1}\boldsymbol{T}(\theta_i)\boldsymbol{T}(\Delta\boldsymbol{\vartheta}_i)\right]{}_{E}^{N}\boldsymbol{T} \tag{30}$$

where $\boldsymbol{T}(\Delta\boldsymbol{\vartheta}_i)$ denotes flexible deformation matrix, in which $\Delta\boldsymbol{\vartheta}_i = (\Delta\gamma_{x_i}, \Delta\gamma_{y_i}, \Delta\gamma_{z_i}, \Delta x_i, \Delta y_i, \Delta z_i)^{\mathrm{T}}$ represents three rotational deformations and three linear deformations, respectively. According to (29) and (30), the positioning error model can be obtained as

$$\begin{aligned}\Delta P &= \left\|\boldsymbol{P} - \boldsymbol{P}'\right\|_2 \\ &= f(\boldsymbol{\theta}, \Delta\boldsymbol{\vartheta})\end{aligned} \tag{31}$$

where $\boldsymbol{\theta} = (\theta_1, \cdots, \theta_N)^{\mathrm{T}}$ and $\Delta\boldsymbol{\vartheta} = (\Delta\vartheta_1, \cdots, \Delta\vartheta_N)^{\mathrm{T}}$.

Appendix B
The Method of Proposed Pose Compensation for Industrial Robots Based on Three Positioning Errors

As shown in Fig. 18(a), there is a part assembled using a robot, and the desired assembly pose (dashed line) and actual pose (solid line) caused by the joint flexible deformation are shown in Fig. 18(b), respectively. Three locations $\boldsymbol{p}_1$, $\boldsymbol{p}_2$, and $\boldsymbol{p}_3$ at the robot's end tool are selected. Then, the predicted positions $\boldsymbol{p}_1'$, $\boldsymbol{p}_2'$, and $\boldsymbol{p}_3'$ of the three locations due to deformation are calculated by the established flexibility error model as follows:

$$\boldsymbol{p}_1' = \Delta\boldsymbol{p}_1^c + \boldsymbol{p}_1, \quad \boldsymbol{p}_2' = \Delta\boldsymbol{p}_2^c + \boldsymbol{p}_2, \quad \boldsymbol{p}_3' = \Delta\boldsymbol{p}_3^c + \boldsymbol{p}_3 \tag{32}$$

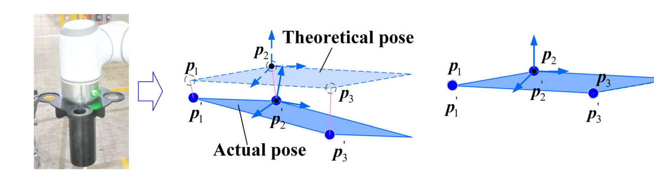
where $\Delta\boldsymbol{p}_1^c$, $\Delta\boldsymbol{p}_2^c$ and $\Delta\boldsymbol{p}_3^c$ denote the predicted flexible errors by (21) for three locations, respectively. According to the robot's kinematic model (31), an equation for inverse solution is constructed as

$$\begin{aligned}&\left\|\boldsymbol{p}_1' - \boldsymbol{T}(\boldsymbol{\Theta} + \Delta\boldsymbol{\Theta})\boldsymbol{p}_{E1}\right\|_2 + \left\|\boldsymbol{p}_2' - \boldsymbol{T}(\boldsymbol{\Theta} + \Delta\boldsymbol{\Theta})\boldsymbol{p}_{E2}\right\|_2 \\ &\quad + \left\|\boldsymbol{p}_3' - \boldsymbol{T}(\boldsymbol{\Theta} + \Delta\boldsymbol{\Theta})\boldsymbol{p}_{E3}\right\|_2 = 0\end{aligned} \tag{33}$$

where $\boldsymbol{T}(\boldsymbol{\Theta})$ is the kinematic model (29), and $\boldsymbol{p}_{E1}$, $\boldsymbol{p}_{E1}$ and $\boldsymbol{p}_{E3}$ represent the positions of the three locations in the end effector coordinate system of the robot, respectively. The joint angle $\boldsymbol{\Theta} + \Delta\boldsymbol{\Theta}$ in the kinematic model $\boldsymbol{T}(\boldsymbol{\Theta})$ corresponds to the deformed pose. According to (33), the joint angle error $\Delta\boldsymbol{\Theta}$ corresponding to the positioning error $\Delta\boldsymbol{p}_1^c$, $\Delta\boldsymbol{p}_2^c$, and $\Delta\boldsymbol{p}_3^c$ can be solved by using the particle swarm optimization (PSO) algorithm [36]. Then, the joint angle after compensation is calculated by

$$\boldsymbol{\Theta}^* = \boldsymbol{\Theta} - \Delta\boldsymbol{\Theta} \tag{34}$$

The desired pose can be reached by inputting the calculated joint angle $\boldsymbol{\Theta}^*$ into the robot, thereby compensating for the assembly pose error caused by the insufficient stiffness of robots.



(a) Assembly part. (b) Theoretical and actual pose. (c) Error compensation for three positions Simultaneously.

Fig. 18. Schematic diagram of pose error compensation.

APPENDIX C
CONVENTIONAL FLEXIBILITY MODELS

The traditional models are as follows, where only the matrix dimensions are provided here for calculating complexity. The specific meanings of parameters can be found in the corresponding literature.

Model I [7]:

$$\Delta \boldsymbol{p} = \boldsymbol{J}_q \boldsymbol{K}_q^{-1} \boldsymbol{J}_q^{\mathrm{T}} \boldsymbol{w} \tag{35}$$

where $\Delta \boldsymbol{p} \in \mathbb{R}^{3\times 1}$, $\boldsymbol{J}_q \in \mathbb{R}^{3\times N}$, $\boldsymbol{K}_q^{-1} = \mathrm{diag}(C_{q1}, \cdots, C_{qN}) \in \mathbb{R}^{N\times N}$, $\boldsymbol{w} \in \mathbb{R}^{3\times 1}$.

Model II [17]:

$$\Delta \boldsymbol{p} = (\boldsymbol{J}_q \boldsymbol{C}_q \boldsymbol{J}_q{}^{\mathrm{T}})\boldsymbol{w} + \sum\nolimits_{i=0}^{N} \left(\boldsymbol{J}_\theta^{(i)} \boldsymbol{C}_\theta^{(i)} \boldsymbol{J}_\theta^{(i)\mathrm{T}}\right)\boldsymbol{w} \tag{36}$$

where $\Delta \boldsymbol{p} \in \mathbb{R}^{3\times 1}$, $\boldsymbol{J}_q \in \mathbb{R}^{3\times N}$, $\boldsymbol{C}_q = \mathrm{diag}(C_{q1}, \cdots, C_{qN}) \in \mathbb{R}^{N\times N}$, $\boldsymbol{w} \in \mathbb{R}^{3\times 1}$, $\boldsymbol{J}_\theta^{(i)} \in \mathbb{R}^{3\times 6}$, $\boldsymbol{C}_\theta^{(i)} \in \mathbb{R}^{6\times 6}$.

Model III [18]:

$$\Delta \boldsymbol{p} = \sum\nolimits_{i=1}^{N} (\boldsymbol{W}_i \bar{\boldsymbol{C}}_i \boldsymbol{W}_i^{\mathrm{T}}) \boldsymbol{S}_{W,E} + \sum\nolimits_{i=1}^{N} (\boldsymbol{W}_i \bar{\boldsymbol{C}}_i \boldsymbol{W}_i^{\mathrm{T}} \boldsymbol{S}^i{}_{W,G}) + \boldsymbol{W}_2 \bar{\boldsymbol{C}}_2 \boldsymbol{W}_2^{\mathrm{T}} \boldsymbol{S}_{W,C} \tag{37}$$

where $\Delta \boldsymbol{p} \in \mathbb{R}^{6\times 1}$, $\boldsymbol{W}_i \in \mathbb{R}^{6\times 6}$, $\bar{\boldsymbol{C}}_i \in \mathbb{R}^{6\times 6}$, $\boldsymbol{S}_{W,E} \in \mathbb{R}^{6\times 1}$, $\boldsymbol{S}_{W,G} \in \mathbb{R}^{6\times 1}$, $\boldsymbol{S}_{W,C} \in \mathbb{R}^{6\times 1}$.

REFERENCES

[1] M. Amersdorfer and T. Meurer, "Equidistant tool path and Cartesian trajectory planning for robotic machining of curved freeform surfaces," *IEEE Trans. Autom. Sci. Eng.*, vol. 19, no. 4, pp. 3311–3323, Oct. 2022.

[2] M. Xiao, Y. Ding, and G. Yang, "A model-based trajectory planning method for robotic polishing of complex surfaces," *IEEE Trans. Autom. Sci. Eng.*, vol. 19, no. 4, pp. 2890–2903, Oct. 2022.

[3] Y. Jiang, Z. Huang, B. Yang, and W. Yang, "A review of robotic assembly strategies for the full operation procedure: Planning, execution and evaluation," *Robot. Comput.-Integr. Manuf.*, vol. 78, Dec. 2022, Art. no. 102366.

[4] Y. Zhang, X. Zhao, Y. Chen, B. Tao, and H. Ding, "Observer-based variable impedance control using moving horizon estimation for robot machining thin-walled workpieces," *IEEE Trans. Ind. Electron.*, vol. 71, no. 6, pp. 5972–5982, Jun. 2024.

[5] C. Ye, J. Yang, and H. Ding, "High-accuracy prediction and compensation of industrial robot stiffness deformation," *Int. J. Mech. Sci.*, vol. 233, Nov. 2022, Art. no. 107638.

[6] G. Du, Y. Liang, B. Gao, S. Al Otaibi, and D. Li, "A cognitive joint angle compensation system based on self-feedback fuzzy neural network with incremental learning," *IEEE Trans. Ind. Informat.*, vol. 17, no. 4, pp. 2928–2937, Apr. 2021.

[7] M. K. Gonzalez, N. A. Theissen, A. Barrios, and A. Archenti, "Online compliance error compensation system for industrial manipulators in contact applications," *Robot. Comput.-Integr. Manuf.*, vol. 76, Aug. 2022, Art. no. 102305.

[8] G. Wang et al., "Trajectory planning and optimization for robotic machining based on measured point cloud," *IEEE Trans. Robot.*, vol. 38, no. 3, pp. 1621–1637, Jun. 2022, doi: 10.1109/TRO.2021.3108506.

[9] Z.-Y. Liao, Q.-H. Wang, H.-L. Xie, J.-R. Li, X.-F. Zhou, and T.-H. Pan, "Optimization of robot posture and workpiece setup in robotic milling with stiffness threshold," *IEEE/ASME Trans. Mechatronics*, vol. 27, no. 1, pp. 582–593, Feb. 2022.

[10] A. Mekaouche, F. Chapelle, and X. Balandraud, "FEM-based generation of stiffness maps," *IEEE Trans. Robot.*, vol. 31, no. 1, pp. 217–222, Feb. 2015.

[11] A. Klimchik, A. Pashkevich, and D. Chablat, "Fundamentals of manipulator stiffness modeling using matrix structural analysis," *Mechanism Mach. Theory*, vol. 133, pp. 365–394, Mar. 2019.

[12] J. Salisbury, "Active stiffness control of a manipulator in Cartesian coordinates," in *Proc. 19th IEEE Conf. Decis. Control Including Symp. Adapt. Processes*, Dec. 1980, pp. 95–100.

[13] S.-F. Chen and I. Kao, "Geometrical approach to the conservative congruence transformation (CCT) for robotic stiffness control," in *Proc. IEEE Int. Conf. Robot. Autom.*, Aug. 2002, pp. 544–549.

[14] G. Alici and B. Shirinzadeh, "Enhanced stiffness modeling, identification and characterization for robot manipulators," *IEEE Trans. Robot.*, vol. 21, no. 4, pp. 554–564, Aug. 2005.

[15] C. Dumas, S. Caro, S. Garnier, and B. Furet, "Joint stiffness identification of six-revolute industrial serial robots," *Robot. Comput.-Integr. Manuf.*, vol. 27, no. 4, pp. 881–888, Aug. 2011.

[16] A. Pashkevich, A. Klimchik, and D. Chablat, "Enhanced stiffness modeling of manipulators with passive joints," *Mechanism Mach. Theory*, vol. 46, no. 5, pp. 662–679, May 2011.

[17] A. Klimchik, B. Furet, S. Caro, and A. Pashkevich, "Identification of the manipulator stiffness model parameters in industrial environment," *Mechanism Mach. Theory*, vol. 90, pp. 1–22, Aug. 2015.

[18] P. Xu et al., "Stiffness modeling of an industrial robot with a gravity compensator considering link weights," *Mechanism Mach. Theory*, vol. 161, Jul. 2021, Art. no. 104331.

[19] W. Zhu, G. Li, H. Dong, and Y. Ke, "Positioning error compensation on two-dimensional manifold for robotic machining," *Robot. Comput.-Integr. Manuf.*, vol. 59, pp. 394–405, Oct. 2019.

[20] G. Xiong, Y. Ding, and L. Zhu, "Stiffness-based pose optimization of an industrial robot for five-axis milling," *Robot. Comput.-Integr. Manuf.*, vol. 55, pp. 19–28, Feb. 2019, doi: 10.1016/j.rcim.2018.07.001.

[21] G. Gao, G. Sun, J. Na, Y. Guo, and X. Wu, "Structural parameter identification for 6 DOF industrial robots," *Mech. Syst. Signal Process.*, vol. 113, pp. 145–155, Dec. 2018.

[22] Z. Liu, A. G. Banerjee, and Y. Choe, "Identifying the influential inputs for network output variance using sparse polynomial chaos expansion," *IEEE Trans. Autom. Sci. Eng.*, vol. 18, no. 3, pp. 1026–1036, Jul. 2021.

[23] J. Wei, C. Chen, and G. Dong, "Global sensitivity analysis for impedance spectrum identification of lithium-ion batteries using time-domain response," *IEEE Trans. Ind. Electron.*, vol. 70, no. 4, pp. 3825–3835, Apr. 2023.

[24] S.-M. Nasiri, R. Hosseini, and H. Moradi, "Novel parameterization for Gauss–Newton methods in 3-D pose graph optimization," *IEEE Trans. Robot.*, vol. 37, no. 3, pp. 780–797, Jun. 2021.

[25] C. Zhao, H. Guo, D. Zhang, R. Liu, B. Li, and Z. Deng, "Stiffness modeling of n(3RRIS) reconfigurable series-parallel manipulators by combining virtual joint method and matrix structural analysis," *Mechanism Mach. Theory*, vol. 152, Oct. 2020, Art. no. 103960.

[26] Z.-Y. Liao, J.-R. Li, H.-L. Xie, Q.-H. Wang, and X.-F. Zhou, "Region-based toolpath generation for robotic milling of freeform surfaces with stiffness optimization," *Robot. Comput.-Integr. Manuf.*, vol. 64, Aug. 2020, Art. no. 101953.

[27] Y. Li, G. Gao, and F. Liu, "Positioning error compensation for industrial robots based on stiffness modelling," *Complexity*, vol. 2020, pp. 1–13, Nov. 2020.

[28] T. Sun, B. Lian, S. Yang, and Y. Song, "Kinematic calibration of serial and parallel robots based on finite and instantaneous screw theory," *IEEE Trans. Robot.*, vol. 36, no. 3, pp. 816–834, Jun. 2020.

[29] A. Wahrburg, J. Bos, K. D. Listmann, F. Dai, B. Matthias, and H. Ding, "Motor-current-based estimation of Cartesian contact forces and torques for robotic manipulators and its application to force control," *IEEE Trans. Autom. Sci. Eng.* , vol. 15, no. 2, pp. 879–886, Apr. 2018.

[30] H. Zhang, S. Ahmad, and G. Liu, "Modeling of torsional compliance and hysteresis behaviors in harmonic drives," *IEEE/ASME Trans. Mechatronics*, vol. 20, no. 1, pp. 178–185, Feb. 2015.

[31] M. M. Alam et al., "Inclusion of bidirectional angular positioning deviations in the kinematic model of a six-DOF articulated robot for static volumetric error compensation," *IEEE/ASME Trans. Mechatronics*, vol. 27, no. 6, pp. 4339–4349, Dec. 2022.

[32] Q. Fan, B. Tao, Z. Gong, X. Zhao, and H. Ding, "Fast global collision detection method based on feature-point-set for robotic machining of large complex components," *IEEE Trans. Autom. Sci. Eng.*, vol. 20, no. 1, pp. 470–481, Jan. 2023.

[33] L. Xu, D. Zhang, J. Xu, R. Wang, and Y. Sun, "A stiffness matching-based deformation errors control strategy for dual-robot collaborative machining of thin-walled parts," *Robot. Comput.-Integr. Manuf.*, vol. 88, Aug. 2024, Art. no. 102726.

[34] M. Raessa, J. C. Y. Chen, W. Wan, and K. Harada, "Human-in-the-loop robotic manipulation planning for collaborative assembly," *IEEE Trans. Autom. Sci. Eng.*, vol. 17, no. 4, pp. 1800–1813, Oct. 2020.

[35] H. Bettahar, O. Lehmann, C. Clévy, N. Courjal, and P. Lutz, "6-DoF full robotic calibration based on 1-D interferometric measurements for microscale and nanoscale applications," *IEEE Trans. Autom. Sci. Eng.*, vol. 19, no. 1, pp. 348–359, Jan. 2022.

[36] X. Chen and Q. Zhan, "The kinematic calibration of an industrial robot with an improved beetle swarm optimization algorithm," *IEEE Robot. Autom. Lett.*, vol. 7, no. 2, pp. 4694–4701, Apr. 2022.



Yingjie Li received the B.Sc. degree in mechanical engineering from Kunming University of Science and Technology, Kunming, China, in 2017, where he is currently pursuing the Ph.D. degree with the Faculty of Mechanical and Electrical Engineering.

His main research interests include kinematic calibration and compensation for flexibility errors caused by external payloads to improve the absolute accuracy of industrial robots.



Guanbin Gao (Member, IEEE) received the B.Sc. and M.Sc. degrees in mechanical engineering and automation from Northeastern University, Shenyang, China, in 2001 and 2004, respectively, and the Ph.D. degree in mechanical manufacturing and automation from Zhejiang University, Hangzhou, China, in 2010.

His current research interests include precision measuring and control, kinematics of industrial robots, and NNs.



Jing Na (Member, IEEE) received the B.Sc. degree in automation and the Ph.D. degree in control science and engineering from the School of Automation, Beijing Institute of Technology, Beijing, China, in 2004 and 2010, respectively.

Since 2010, he has been with the Faculty of Mechanical and Electrical Engineering, Kunming University of Science and Technology, Kunming, China, where he became a Professor in 2013. From 2011 to 2013, he was a Monaco/ITER Post-Doctoral Fellow with ITER Organization, Saint-Paul-lès-Durance, France. From 2015 to 2017, he was a Marie Curie Fellow with the Department of Mechanical Engineering, University of Bristol, U.K. He has coauthored one monograph and more than 100 international journal articles and conference papers. His research interests include intelligent control, adaptive parameter estimation, nonlinear control and applications for robotics, vehicle systems, and wave energy convertor. He received the Best Application Paper Award from the IFAC ICONS 2013 and the 2017 Hsue-Shen Tsien Paper Award. He has served as the Organization Committee Chair for DDCLS 2019 and the International Program Committee Chair for ICMIC 2017. He is an Associate Editor of IEEE TRANSACTIONS ON INDUSTRIAL ELECTRONICS and *Neurocomputing*.



Yashan Xing (Member, IEEE) was born in Yunnan, China. She received the B.Sc. degree in mechanical engineering from Kunming University of Science and Technology, Yunnan, in 2014, the M.Sc. degree in mechanical engineering from Blekinge Tekniska Högskola, Blekinge, Sweden, and Kunming University of Science and Technology, in 2017, and the Ph.D. degree in control engineering from the Universitat Politècnica de Catalunya, Barcelona, Spain.

Her current research interests include modeling, adaptive control, and parameter estimation for solid oxide fuel cells and solid oxide electrolysis cells.